



1 **Holocene sea ice and paleoenvironment conditions in the**
2 **Beaufort Sea (Canadian Arctic) reconstructed with lipid**
3 **biomarkers**

4 Madeleine Santos^{1,2}, Lisa Bröder¹, Matt O'Regan^{3,4}, Iván Hernández-Almeida^{1,5}, Tommaso Tesi⁶,
5 Lukas Bigler^{1,7}, Negar Haghipour^{1,8}, Daniel B. Nelson², Michael Fritz⁹, Julie Lattaud^{1,2,7}

6 ¹Department of Earth and Planetary Sciences, ETHZ, Zurich, 8092 Switzerland

7 ²Department of Environmental Science, University of Basel, Basel, 4056, Switzerland

8 ³Department of Geological Sciences, Stockholm University, Stockholm, 106 91, Sweden

9 ⁴Bolin Centre for Climate Research, – Stockholm University, Stockholm, 106 91, Sweden

10 ⁵Past Global Changes, University of Bern, Bern, 3012, Switzerland

11 ⁶Institute of Polar Sciences (ISP), Bologna, 40129, Bologna 40128, Italy

12 ⁷Department of Environmental Science, Stockholm University, Stockholm, 106 91, Sweden

13 ⁸Laboratory of Ion Beam Physics, ETHZ, Zurich, 8092, Switzerland

14 ⁹Alfred Wegener Institute, Helmholtz Centre for Polar and Marine Research, Potsdam, 14473, Germany

15

16 *Correspondence to:* Julie Lattaud (Julie.lattaud@aces.su.se)



Abstract The Beaufort Sea region in the Canadian Arctic has undergone substantial sea ice loss in recent decades, primarily driven by anthropogenic climate warming. To place these changes within the context of natural climate variability, Holocene sea ice evolution and environmental conditions (sea surface temperature, salinity, terrestrial input) were reconstructed using lipid biomarkers (IP₂₅, and other HBIs, OH-GDGT, brGDGT, C_{16:0} fatty acid, phytosterols) from two marine sediment cores collected from the Beaufort Shelf and slope, spanning the past 9.1 ka and 13.3 cal kyr BP, respectively. The Early Holocene (12-8.5 ka) is characterized by relatively higher sea surface temperature, lower salinity and no spring/summer sea ice until 8.5 ka on the Beaufort Sea slope. Around 8.5 ka, a peak in organic matter content is linked to both increased terrestrial input and primary production and may indicate increased riverine input from the Mackenzie River and terrestrial matter input from coastal erosion. Following this period, terrestrial inputs decreased throughout the Middle Holocene in both cores. A gradual increase in IP₂₅ and HBI-II concentrations aligns with relatively higher salinity, lower sea surface temperature and rising sea levels, and indicate the establishment of seasonal (spring) sea ice on the outer shelf around 7 ka and on the shelf around 5 ka. These patterns suggest an expansion of the sea ice cover beginning in the Middle Holocene, influenced by decreasing summer insolation. During the Late Holocene (4–1 ka), permanent sea ice conditions are inferred on the slope with a peak during the Little Ice Age. After 1 ka, seasonal sea ice conditions on the slope are observed again, alongside an increase in salinity and terrestrial input, and variable primary productivity. Similar patterns of Holocene sea ice variability have been observed across other Arctic marginal seas, highlighting a consistent response to external climate forcing. Continued warming may drive the Beaufort Sea toward predominantly ice-free conditions, resembling those inferred for the Early Holocene.



37 1. Introduction

38 Sea ice is a critical component of the Arctic climate system, influencing ocean–atmosphere interactions, modulating
39 surface albedo (Kashiwase et al., 2017), regulating heat fluxes (Lake, 1967), and influencing ecosystem structure
40 through its control on light penetration and nutrient cycling (Lannuzel et al., 2020). Its high sensitivity to temperature
41 makes it both a driver and indicator of Arctic climate change. Since the late 1970s, satellite observations have revealed
42 a significant decline in Arctic sea ice extent, sparking renewed interest in the mechanisms that govern sea ice
43 variability over multiple timescales (Stroeve et al., 2012). The Canadian Beaufort Sea is a marginal sea of the western
44 Arctic Ocean which exhibits strong seasonal and interannual variability in sea ice cover. Characterized by landfast ice
45 on the shelf and mobile pack ice offshore, this region has experienced significant sea-ice loss in recent decades due to
46 rising atmospheric and oceanic temperatures (Carmack et al., 2015; Comiso et al., 2008).

47 Understanding the natural variability of sea-ice prior to the industrial era is critical for contextualizing recent trends.
48 Throughout the Holocene, Arctic sea ice has responded to changes in orbital forcing, ocean circulation, and ice sheet
49 dynamics (Park et al., 2018; Stein et al., 2017). The enhanced meltwater discharge and re-routing following the
50 retreat of the Laurentide Ice Sheet (LIS), fully deglaciated by approximately 6.7 ± 0.4 ka (Ullman et al., 2016),
51 contributed to oceanographic shifts and transient cooling events, such as the Younger Dryas (~ 12.8 – 11.7 ka)
52 (Broecker et al., 1989). Lipid biomarker records and climate simulations suggest reduced sea ice during the Early
53 Holocene thermal maximum (11–9 ka), followed by expansion through the Middle to Late Holocene, consistent with
54 declining summer insolation (Stranne et al., 2014; Wu et al., 2020). Numerous studies on Arctic sea ice variability
55 have focused on a single offshore location, often neglecting the spatial extent of sea ice cover toward the coast and
56 the migration of the marginal ice zone.

57 Sea-ice cover is controlled by both the atmosphere and the ocean, including salinity, sea temperature and freshwater
58 influence, which are parameters that can be challenging to reconstruct in polar environments. Biomarker lipids and
59 their ratios are a useful toolkit, with compound-specific hydrogen isotopes of phytoplankton biomarkers a promising
60 tool for salinity reconstruction (e.g., Lattaud et al., 2019; Sachs et al., 2018; Weiss et al., 2019). However, in the
61 Arctic Ocean low abundances of biomarker restricts the application of this method to the dominant biomarkers
62 present such as palmitic acid ($C_{16:0}$ fatty acid, Sachs et al., 2018). Several proxies for sea temperature exist using
63 microfossils (e.g., dinocyst assemblages, e.g., Richerol et al., 2008), inorganic ratios (e.g., Mg/Ca of foraminifera,



e.g., Barrientos et al., 2018; Kristjánsdóttir et al., 2007) and lipid biomarkers (e.g., Ruan et al., 2017; Varma et al., 2024). Lipid biomarker proxies developed for reconstruction of cold water ($< 15^{\circ}\text{C}$) temperature variations usually include hydroxylated glycerol dialkyl glycerol tetraether (OH-GDGT) (Lü et al., 2015; Varma et al., 2024). However, even the latest calibration of Varma et al. (2025) using a combination of OH-GDGT and isoprenoid GDGT (isoGDGT) shows high variability at low temperature. In addition, representability of polar core-tops sediment in the global calibration dataset is strongly biased toward the European and Russian Arctic.

This study presents a multi-proxy reconstruction of Holocene sea ice and oceanographic variability from two sediment cores (PCB09, PCB11) collected from the Beaufort outer shelf and shelf slope. Lipid biomarkers, including highly branched isoprenoids (HBIs), glycerol dialkyl glycerol tetraethers (GDGTs), the hydrogen isotopic compositions of algal-derived fatty acids and terrestrial sterols, are used to reconstruct sea-ice cover, sea surface temperatures (SSTs), salinity and terrestrial organic matter input. Additionally, a set of surface sediments is used to assess the applicability and calibrate salinity and sea temperature proxies in sediments of the Beaufort Sea.

The primary objectives are to (1) reconstruct the spatial evolution of sea ice cover on the Beaufort Shelf throughout the Holocene, (2) evaluate the influence of insolation, meltwater inputs, and oceanic forcing on regional sea ice dynamics, and (3) contribute to a broader understanding of Arctic climate variability in the context of ongoing and future climate change.

2. Material and Methods

2.1. Study area

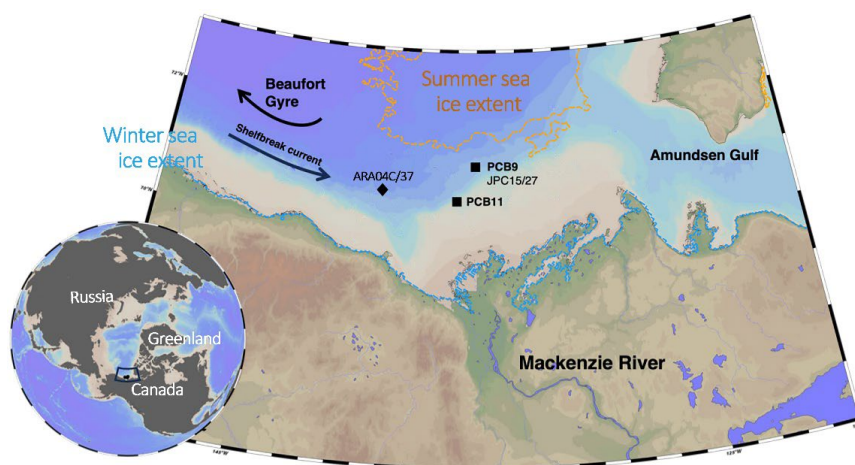
The study focuses on the Canadian Beaufort Sea, one of the marginal seas of the Arctic Ocean (Fig. 1), bounded by the glacially excavated Amundsen Gulf to the east, Mackenzie Trough to the west, and the Mackenzie River delta to the south (Carmack et al., 2004). The shelf is a large estuarine setting at the interface between the Arctic Ocean and the Mackenzie River (Omstedt et al., 1994) (Fig.1). The Mackenzie River is a significant source of freshwater to the Beaufort Sea, with an annual water discharge of $316 \text{ km}^3 \text{ yr}^{-1}$ (Holmes et al., 2012) and is considered the largest Arctic river in terms of sediment flux ($124\text{--}128 \text{ Mt}\cdot\text{yr}^{-1}$) (Stein et al., 2004). At the same time, permafrost coastal erosion adds another $8\text{--}9 \text{ Mt}\cdot\text{yr}^{-1}$ of sediment into the Beaufort Sea, including carbon and nutrients (Wegner et al., 2015). Surface water circulation in the Beaufort Sea is primarily characterized by the clockwise Beaufort Gyre,



90 which drives offshore currents towards the west and traps the majority of the Arctic Ocean's freshwater in the
91 Canada Basin (Serreze et al., 2006). There is also a eastward flowing shelf-break current at depths beneath 50 m,
92 which transports Pacific Water (coming from the Bering Strait) along the slope (Pickart, 2004). Sea ice cover on the
93 Beaufort Shelf north of the Mackenzie River Delta varies from year to year, but generally begins to form in mid-
94 October, persisting until ice break up in April-May (Fig. S1). During ice break up, an open water flaw leads occur
95 along the outer edge of the landfast ice allowing the formation of a spring marginal zone.

96 2.2. Material

97 Two sediment cores were analyzed in the study. They were recovered as part of the Permafrost Carbon on the
98 Beaufort Shelf (*PeCaBeau*) project during the 4th Leg of the 2021 CCGS Amundsen expedition (Bröder et al., 2022,
99 Fig.1). At station PCB09 (71.1°N, 135.1°W) at a water depth of 675 m on the Beaufort shelf slope, a piston core
100 (PC, length of 420 cm) and multi core (MC, 30 cm) were retrieved (Fig. 1). At station PCB11 (70.6°N, 136.0°W) on
101 the outer Beaufort shelf (74 m water depth) a giant gravity core (GGC, length of 290 cm) and MC (32 cm) were
102 recovered (Fig. 1). PCB09 is found within the modern Atlantic bottom water mass, while PCB11 lies within the
103 Pacific summer water (Fig. S2), the water masses were defined as in (Matsuoka et al., 2012). The core tops (0-1cm)
104 from 22 multicores collected during *PeCaBeau*, were used to ground truth the hydrogen isotope ratio of C_{16:0} fatty
105 acid proxy for reconstructing salinity (Fig. S1).



106

107 Figure 1: Combined topographic and bathymetric map of the Beaufort Shelf region (Canadian Arctic) displaying the
108 cores from this study as black squares (PCB09 and PCB11) and key records discussed in the text (ARA04C/37 from



109 Wu et al., 2020; JPC15/27 from Keigwin et al., 2018). The modern summer (orange dotted line) sea-ice extent is
110 shown, the winter sea ice extent follows the coastline. Map generated using Ocean Data View (Schlitzer, 2025).

111 2.3. Methods

112 2.3.1. Core processing

113 During the PeCaBeau expedition, all cores were scanned shipboard on a Geotek multi-sensor core logger (MSCL).
114 Bulk density and magnetic susceptibility were measured at a 1 cm downcore resolution on the piston and gravity cores,
115 (Bröder et al., 2022). The cores remained unopened and were shipped to AWI Potsdam following the expedition. They
116 were subsequently split in the fall/winter and the working halves sampled using 2x2 cm u-channels, before being cut
117 into 1-2 cm thick slices which were frozen and freeze dried.

118 An ITRAX XRF-core scanner was used to measure relative elemental abundances at Stockholm University, Sweden.
119 Measurements were performed on u-channel samples at a downcore resolution of 2 mm. Analyses were made using a
120 Mo tube at a voltage of 55 kV, a current of 50 mA and an exposure time of 20 s. Here we present the ratios of Ca/Ti,
121 reflecting detrital carbon inputs regionally elevated by meltwater delivery from either the Mackenzie or Amundsen
122 Gulf during deglaciation (Klotsko et al., 2019; Swärd et al., 2022; J. Wu et al., 2020). Zr/Rb was used as a proxy for
123 grain size variations (L. Wu et al., 2020) and Br/Cl as a proxy for marine organic matter (Wang et al., 2019).

124 2.3.2. Age model

125 The chronology of the piston and gravity cores (Fig. 2) were determined by ^{14}C dating of foraminifera ($n = 13$,
126 PCB09) and bivalve shells ($n = 7$, PCB11) (Table S1). The MSCL data was used to stratigraphically correlate
127 PCB09 with JPC15/27 (Keigwin et al., 2018) allowing us to integrate existing radiocarbon ages ($n=8$) from this
128 record with our new data ($n=5$) (Fig. S3).

129 Bivalve shells were either picked from the split cores when sampling, or later from the freeze-dried sediments.
130 Foraminifera were picked from the $>45\ \mu\text{m}$ fraction of the wet-sieved samples following organic extractions.
131 Foraminifera samples consisted of either planktonic (*Neogloboquadrina pachyderma*), benthic, or a combination of
132 both in horizons when specimens were extremely rare. Care was given to pick well preserved foraminifera to avoid
133 age bias (Wollenburg et al., 2023). Foraminifera and mollusk samples were prepared for Accelerator Mass



134 Spectrometry (AMS) analyses at the Laboratory for Ion Beam Physics at ETHZ using procedures described in
135 (Missiaen et al., 2020) which include sieving and acid cleaning to remove impurities from the shells.

136 Radiocarbon-based age models were generated using the BACON package in R (Blaauw & Christen, 2011) and the
137 Marine20 calibration curve (Heaton et al., 2020). A reservoir age of 330 ± 41 years was applied to the Holocene-age
138 mollusc samples in PCB11 as determined by (West et al., 2022) for Pacific waters entering the Arctic Ocean in the
139 Chukchi Sea. For PCB09 we applied the approach used (Keigwin et al., 2018) for JPC15/27 and (J. Wu et al., 2020)
140 for ARA04C/37 but updated for Marine20 as described by (Lin et al., 2025). A reservoir correction of -150 ± 100
141 years was applied to Holocene planktic foraminifera, and a larger reservoir correction (50 ± 100 years) for the
142 bottom 4 samples (Table S1) that fall within the Younger Dryas. In our age model we also incorporate samples of
143 benthic foraminifera that were calibrated using a reservoir correction of 206 ± 67 years, determined by (West et al.,
144 2022) for Atlantic waters near the Chukchi Sea. Samples containing mixed planktic and benthic foraminifera were
145 calibrated using an average of these values (28 ± 85 years).

146 **2.3.3. Bulk organic matter**

147 For the determination of total organic carbon (TOC) content and stable carbon isotope composition ($\delta^{13}\text{C}$) at the
148 University of Basel, about 12 mg of freeze-dried sediment was weighed into each silver capsule and 1-2 drops of
149 distilled water were added. The samples were exposed to fuming hydrochloric acid (HCl, 37%) in a desiccator for 24
150 hours to remove inorganic carbon. Samples were dried (48 h, 50 °C) and analyzed using an elemental analyser
151 coupled to an isotope mass spectrometer (Sercon, Integra 2). The standards used to calculate TOC was
152 Ethylenediaminetetraacetic acid (EDTA, Sigma Aldrich) and for $\delta^{13}\text{C}$ were USGS40 ($-26.389 \pm 0.042\text{‰}$, IAEA),
153 USGS64 (-40.81 ± 0.04 , IAEA), and USGS65 (-20.29 ± 0.04 , IAEA). The analytical precision, defined as the standard
154 deviation of the measurement of the USGS standards for the $\delta^{13}\text{C}$ sequence was $\pm 0.03\text{‰}$.

155 **2.3.4. Biomarkers**

156 5 g of homogenized freeze-dried sediment was extracted using an Energy Dispersive Guided Extraction (EDGE)
157 following (Lattaud, Bröder, et al., 2021). Briefly, after extraction with dichloromethane (DCM): Methanol (9:1, v/v),
158 the total lipid extracts (TLE) were saponified at 70 °C for two hours. The neutral phase was collected by liquid-
159 liquid extraction with 10 mL of hexane, three times. The leftover TLE was acidified to pH 2 and the acid phase was



recovered by liquid-liquid extraction adding 10 mL hexane:DCM (4:1, v/v), three times. The acid compounds were methylated by adding MeOH:HCl (95:5, v/v) and heated at 70°C overnight. The methylated fatty acids were recovered by liquid-liquid extraction (three times) with 10 mL hexane:DCM (4:1, v/v). Internal standards were added to the neutral fraction prior to silica chromatography: 7-hexylnonadecane (7-HND, provided by S. Belt), 9-octylheptadec-8-ene (9-OHD, provided by S. Belt), C₂₂ 5,16-diol (Interbioscreen), C_{36:0} alkane (Sigma Aldrich) and C₄₆ (Huguet et al., 2006). The neutral phase was separated into three fractions (F1, F2, and F3) through silica column (combusted and deactivated 1%) using hexane:DCM (9:1, v/v), DCM, and DCM: Methanol (1:1, v/v). The F1 containing HBIs was analyzed on a GC-MS (Agilent 7890-5977A) operating in Selective Ion Monitoring (SIM) mode at the Institute of Polar Sciences (ISP), Bologna, Italy, following (Belt et al., 2014). The column used was a J&W DB5-MS (length 30 m, id 250 µm, 0.25 µm thickness). Integrations were done in SIM mode for IP₂₅ (m/z = 350) and HBI IV, HBI II (m/z = 348) and HBI III (m/z = 346). Concentration of IP₂₅ were corrected for m/z 348 influence (4 %) and instrumental response factor. 9-OHD was used to quantify HBIs. A reference sediment containing known amount of IP₂₅ was run in parallel to correct IP₂₅ concentration. F3, containing the GDGTs, was filtered using a polytetrafluoroethylene filter (PTFE, 45 µm pore size) and analyzed with high performance liquid chromatography (LC)/atmospheric pressure chemical ionization–MS on an Agilent 1260 Infinity series LC-MS according to (Hopmans et al., 2016) and following (Lattaud, De Jonge, et al., 2021). GDGTs were quantified using the C₄₆ internal standard assuming the same response factor. The F3 fraction was then silylated with bis(trimethylsilyl)trifluoroacetamid (BSTFA) (70 °C 30 min) and analysed at the ISP for sterol concentration on a GC-MS. The C₂₂ 5,16 is used to quantify sterols. Specific m/z ratios have been extracted from chromatograms in order to identify each biomarker according to their respective mass spectra. Lipid δ²H values were analyzed by GC-IRMS on all acid fractions having adequate compound abundance. Samples were analyzed using splitless injection with a split/splitless inlet at 280 °C and a Restek Rtx-5MS GC column (30 m × 0.25 mm × 0.25 µm) with helium carrier gas at 1.4 mL min⁻¹. The GC oven was held at 60°C for 1.5 min, ramped to 140°C at 15°C min⁻¹, then to 325 °C at 4 °C min⁻¹, and held for 15 min. Column effluent was pyrolyzed at 1420°C, and δ²H values were measured on a Thermo Delta V Plus IRMS. The H₃⁺ factor was evaluated with each measurement sequence to confirm stability. Values were always lower than 3 ppm mV⁻¹. Reference standards with known isotopic compositions (Mix A7, USGS71, C_{30:0} FAME; provided by Arndt Schimmelmann, Indiana University, USA) were analyzed alongside samples to normalize values to the Vienna Standard Mean Ocean Water-



Standard Light Antarctic Precipitation (VSMOW-SLAP) scale. Standards were injected at a range of concentrations so that peak size effects could be assessed and corrected for. Quality control samples with known $\delta^2\text{H}$ values were measured as unknowns to check precision and accuracy ($\text{C}_{16:0}$ FAME in mix F₈₋₄₀, $\text{C}_{30:0}$ FAME; Arndt Shimmelmann), which were 4.2 ‰ or better, and 1.0 ‰ or better, respectively ($n = 13-16$). Final fatty acid $\delta^2\text{H}$ values of $\text{C}_{16:0}$ were corrected for added hydrogen during methylation following [Eq. 1].

$$\delta^2\text{H}_{\text{C}_{16:0}} = \frac{(n\text{H}_{\text{FAME}} + n\text{H}_{\text{CH}_3}) \times \delta^2\text{H}_{\text{FAME measured}} - n\text{H}_{\text{CH}_3} \times \delta^2\text{H}_{\text{CH}_3}}{n\text{H}_{\text{FAME}}} \quad (1)$$

Where $n\text{H}_{\text{CH}_3} = 3$, $n\text{H}_{\text{FAME}} = 32$.

2.3.5. Biomarker ratios

In order to describe sea ice variability in the Holocene, the PIP_{25} index is used (Müller et al., 2011). The PIP_{25} index [Eq. 2] uses additional phytoplankton biomarkers (i.e. brassicasterol, dinosterol, and HBI-III) which indicate open water conditions to compare with the abundance of IP_{25} (Belt et al., 2007):

$$\text{PIP}_{25} = \frac{\text{IP}_{25}}{[\text{IP}_{25}] + [\text{Phytoplankton biomarker}] \cdot c} \quad (2)$$

HBI-III was used in this study (Belt et al., 2015; Kolling et al., 2020; Köseoğlu et al., 2018; Smik et al., 2016) as a reference for pelagic phytoplankton to derive $\text{P}_{\text{III}}\text{IP}_{25}$ index (afterward called PIP_{25}). Dinosterol was not detected in the samples, and brassicasterol has been shown to derive mainly from terrestrial input in the region (J. Wu et al., 2020). The c value represents the ratio of the mean concentration of IP_{25} over the mean concentration of HBI-III of all samples for each core.

Surface salinity was reconstructed using the calibration between $\delta^2\text{H}$ of $\text{C}_{16:0}$ fatty acid (palmitic acid) and salinity from the test study of Sachs et al. (2018) [Eq. 3] after testing surface sediments from multicore from the region (Fig. S3):

$$\delta^2\text{H}_{\text{PA}} = 4.22 (\pm 0.6) * \text{Salinity} - 338 (\pm 15) \quad (3)$$

where S is salinity in practical salinity units (PSU). Based on the known calibration errors (4‰ for the $\delta^2\text{H}$ measurement), reconstructed salinity should have an associated error of ± 7 PSU.



To reconstruct sea surface temperature, hydroxylated GDGTs (OH-GDGTs) were used as the hydroxyl group in these GDGTs is suggested to be an adaptation feature to regulate permeability in cold waters (Liu et al., 2012). In this study, the RI-OH' [Eq. 4] and TEX-OH [Eq. 5] indexes were calculated:

$$RI-OH' = \frac{[OH-GDGT-1]+2*[OH-GDGT-2]}{[OH-GDGT-0]+[OH-GDGT-1]+[OH-GDGT-2]} \quad (4)$$

$$TEX-OH = \frac{GDGT-2+GDGT-3+Cren\ isomer}{GDGT-2+GDGT-3+Cren\ isomer+OH-GDGT-0+GDGT-1} \quad (5)$$

For the conversion from RI-OH' and TEX-OH to sea surface temperature (SST), the recent calibration of Varma et al. (2024) is used [Eq. 6 and 7]:

$$RI-OH' = 0.04 \times SST + 0.003 \quad (6)$$

$$TEX-OH = 0.021 \times SST + 0.08 \quad (7)$$

Several organic proxies have been used to interpret terrestrial organic matter input such as branched glycerol dialkyl glycerol tetraether (brGDGTs), long chain *n*-alkanes, and plant sterols. BrGDGTs are membrane lipids synthesized by bacteria and are known to be ubiquitous in terrestrial environments (Schouten et al., 2013). The BIT index (Hopmans et al., 2004) [Eq.8] is a common indicator of terrestrial input into the marine realm:

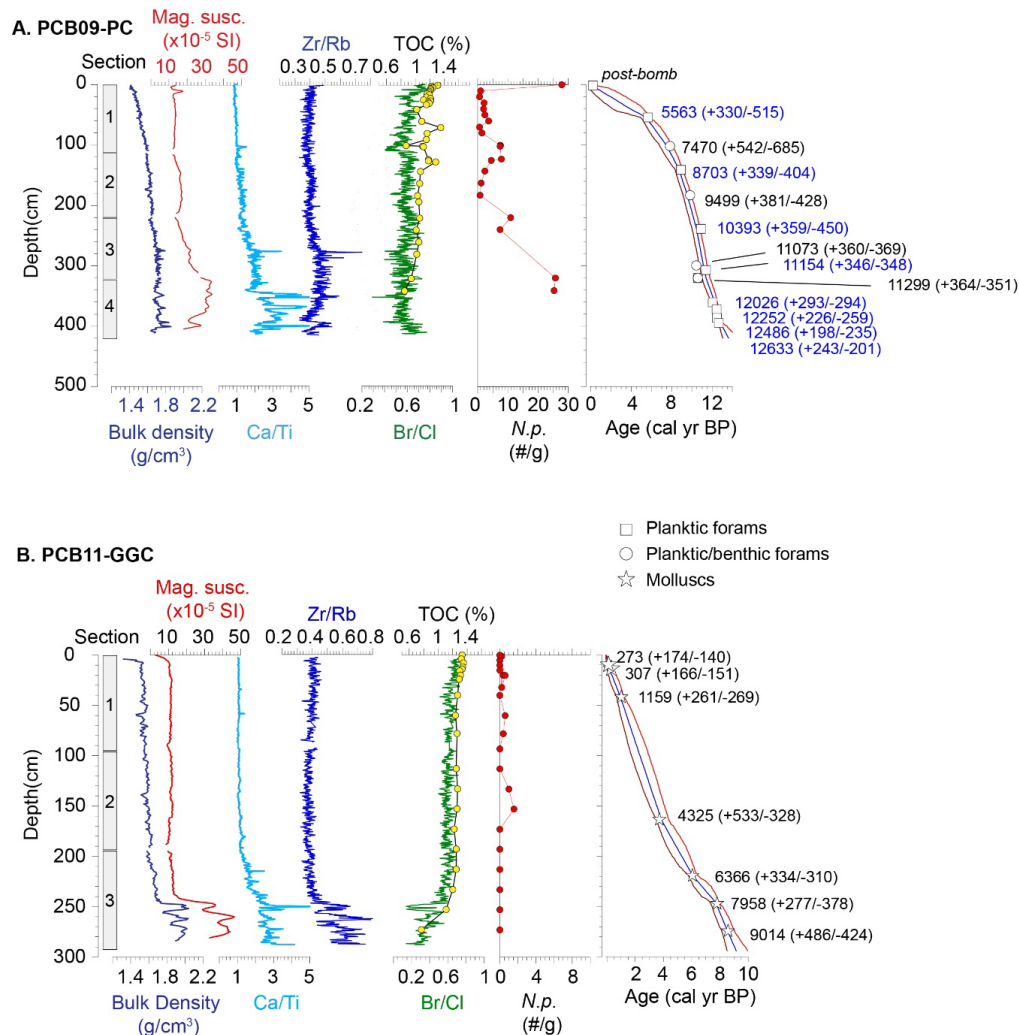
$$BIT = \frac{[BrGDGT-Ia+IIa+IIIa]}{[BrGDGT-Ia+IIa+IIIa]+Crenarcheol} \quad (8)$$

2.3.6. Micropaleontology

Extracted sediments were wet sieved using a 45 µm mesh. The >45 µm fraction was dried in the oven (40 °C) and picked for foraminifera using a stereoscopic microscope. Planktonic foraminifera species are identified (<https://www.mikrotax.org/pforams/>) using the morphological descriptions compiled in Microtax and counted for each sample.



230 3. Results



231

232 **Figure 2:** Core description for (a) PCB09 and (b) PCB11 presenting bulk density, magnetic susceptibility, X-Ray
233 Fluorescence (XRF) results including Ca/Ti, Zr/Rb and Br/Cl ratios. Total organic carbon content (%) and abundance
234 of *N. pachyderma* (*N. p.*, number/gram of sediment) as well as the age models of PCB09 and PCB11 generated using
235 the Bacon Rpackage (Blaauw & Christen, 2011). The red bands illustrate the 95% confidence level around the
236 modelled median age (blue line). Symbols indicate the calibrated age of the dated material before age-modelling. The
237 errors on these are lower than the symbol size. The numbers are the median modelled ages and 95% error at the
238 location of each sample. Blue radiocarbon ages originated from nearby core HLY13-15JPC (Keigwin et al., 2018).



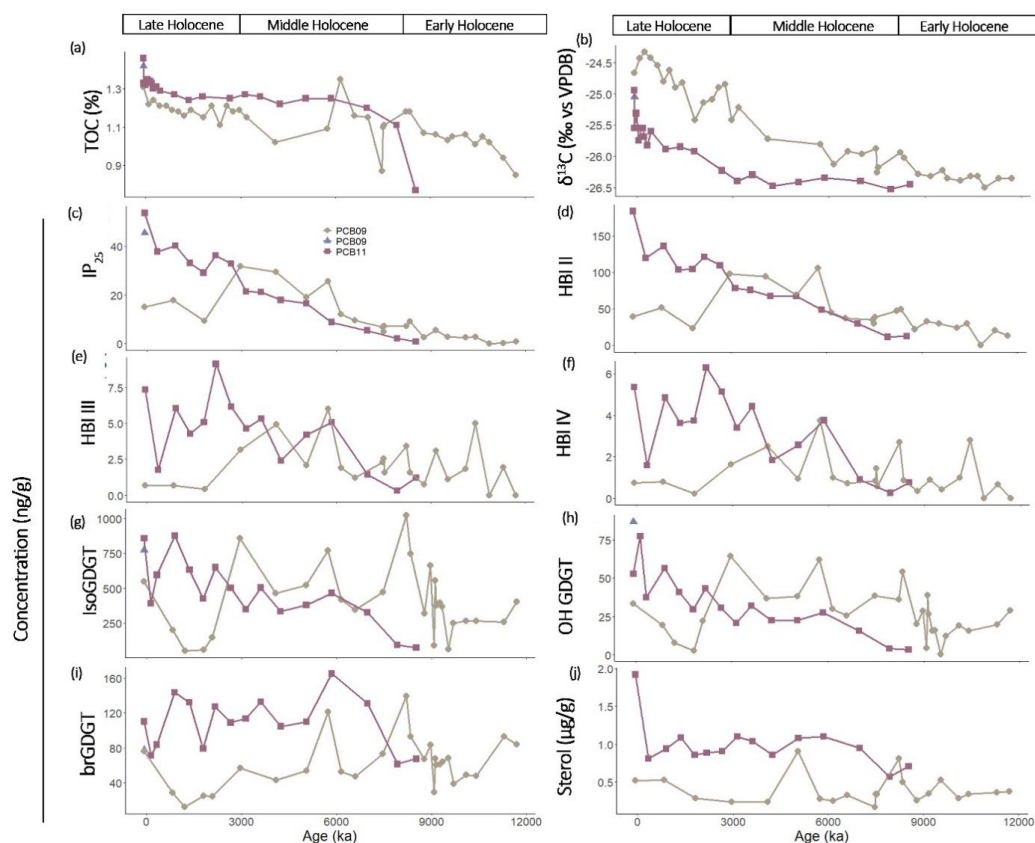
239 3.1. Core chronology, lithostratigraphy and bulk organic matter

240 The age models of cores PCB09 (Fig. 2a) and PCB11 (Fig. 2b) show that they cover the last 13365 ± 687 yr BP and
241 9115 ± 723 yr BP, respectively. PCB11 has a mean sedimentation rate of 35 ± 10 cm kyr⁻¹ with slightly higher
242 sedimentation rates in the Late Holocene (< 4 ka). Conversely, PCB09 has an average sedimentation rate of 50 ± 27
243 cm kyr⁻¹, with substantially higher sedimentation rates before the Late Holocene.

244 The upper 300 cm of PCB09 (0 – 11 ka) display a gradual downcore increase in bulk density, reflecting porosity loss
245 in largely homogenous silty-clay sediments (Fig 2a). Below 300 cm, slightly higher variability in the bulk density,
246 elevated magnetic susceptibility and higher Zr/Rb all point towards a transition to slightly coarser-grained sediments.
247 Ca/Ti tended to increase downcore becoming more variable below 105 cm (7.6 ± 0.6 cal yr BP). There was a notable
248 stepwise increase in Ca/Ti at 345 cm (11.7 ± 0.4 ka, Fig. 2a). Higher detrital carbonate inputs are widely described in
249 deglacial and Early Holocene sediments from the region, and generally associated with meltwater inputs from the
250 Mackenzie River and Amundsen Gulf (Klotsko et al., 2019). Discrete peaks in Zr/Rb and bulk density, indicative of
251 sediment coarsening, co-occurred with elevated Ca/Ti ratios at depths of 276 cm (10.8 ± 0.4 cal yr BP), 345–352 (11.8
252 ± 0.4 cal yr BP) and 402 cm (12.8 ± 0.4 cal yr BP). These events are broadly consistent with the timing of the meltwater
253 discharge events described by (Klotsko et al., 2019; J. Wu et al., 2020) with the oldest two associated with the Younger
254 Dryas and pre-boreal Oscillation.

255 A similar pattern is seen in PCB11, where below 240 cm (7.4 ± 0.6 cal yr BP) there was an abrupt increase in bulk
256 density, magnetic susceptibility, Zr/Rb and Ca/Ti. TOC concentrations and the Br/Cl ratio (which mirrors small scale
257 changes in the TOC) also decreased notably through this interval (Fig. 2b, 3a). This lithologic transition post-dates
258 the deglacial and Early Holocene detrital carbonate inputs in cores recovered from the Beaufort Sea slope (Klotsko et
259 al., 2019). It is likely that this coarser basal facies is related to the inundation of the shelf during transgression.

260 Bulk sediment $\delta^{13}\text{C}$ of PCB09 was lowest in the Early Holocene at approximately -26.3‰ until 8.7 ± 0.4 ka, before
261 increasing during the Middle and Late Holocene to -24.7‰ . The trend in $\delta^{13}\text{C}$ in PCB11 is similar to PCB09
262 showing a steady increase over time from -26.5‰ to -25.8‰ .



263

264 Figure 3: Bulk characteristics and biomarker concentrations (in ng/g_{sediment}) for core PCB09 (brown circles) and
 265 PCB11 (red squares) with (a) total Organic Carbon (TOC), (b) $\delta^{13}\text{C}$, (c) IP_{25} , (d) HBI-II, (e) HBI III, (f) HBI IV, (g)
 266 isoprenoid GDGTs (isoGDGT), (h) hydroxylated GDGTs (OH-GDGT), (i) branched GDGTs (brGDGT) and (j)
 267 terrestrial sterols (sum of brassicasterol, stigmaterol, β -sitosterol, campesterol).

268 3.2. Biomarkers

269 IP_{25} and HBI II ($\text{C}_{25:2}$) concentrations were generally low ($< 2 \text{ ng/g}$) in the Early Holocene (Fig. 3c,d). IP_{25} in both
 270 cores increased throughout the Middle to Late Holocene. During the Late Holocene, IP_{25} and HBI II concentrations
 271 dropped in PCB09 around $1.8 \pm 1.5 \text{ ka}$. Concentrations of both biomarkers were higher in PCB11 than in PCB09
 272 after 3 ka, reaching modern values of 40 ng g^{-1} and 150 ng g^{-1} (IP_{25} and HBI II). PIP_{25} values in both cores increased
 273 from the Early to the Middle Holocene (Fig. 4a). In PCB09, PIP_{25} values decreased around 1 ka before increasing
 274 back to modern values of 0.7.



HBI III ($C_{25:3}$) and HBI IV ($C_{25:4}$) were low in both cores with values below 8 ng g^{-1} (Fig. 3e,f). Concentrations were higher in PCB11 than in PCB09 after 4 ka

The concentration of isoGDGTs and OH-GDGTs followed a similar pattern throughout the Holocene (Fig. 3g,h). IsoGDGTs and OH-GDGT concentrations in PCB09 were stable during the Early Holocene at around 400 ng g^{-1} and 25 ng g^{-1} , respectively. At around 8.5 ka, the isoGDGTs and OH-GDGT amounts doubled. Throughout the Middle Holocene, isoGDGTs and OH-GDGT concentrations were variable but above 500 ng g^{-1} . A drop in PCB09 to almost below detection limits occurred between 1-1.5 ka. IsoGDGTs and OH-GDGTs in PCB11 showed a steady increase from around 100 ng g^{-1} and 10 ng g^{-1} , respectively, in the Early Holocene to $>500 \text{ ng g}^{-1}$ and $>50 \text{ ng g}^{-1}$ (Fig. 3g,h).

BrGDGTs concentrations in PCB09 were below 100 ng g^{-1} throughout the cores except for peaks during the Early and Middle Holocene at 11.2 ± 0.3 , 8.2 ± 0.5 and 5.7 ± 0.5 ka, the latter was also seen in PCB11 (albeit concentrations were higher in PCB11) (Fig. 3i). Terrestrial sterol concentrations in PCB09 were relatively stable throughout the core except for short-lived peaks at 9.5 ± 0.4 , 8.2 ± 0.5 and 5.0 ± 0.9 ka (Fig. 3j). In PCB11, the concentration remained stable throughout the core after an initial increase at 6.9 ± 0.6 ka and a peak in the surface sediment.

3.5. Salinity, sea surface temperature (SST) and terrestrial input inferred from biomarker ratios

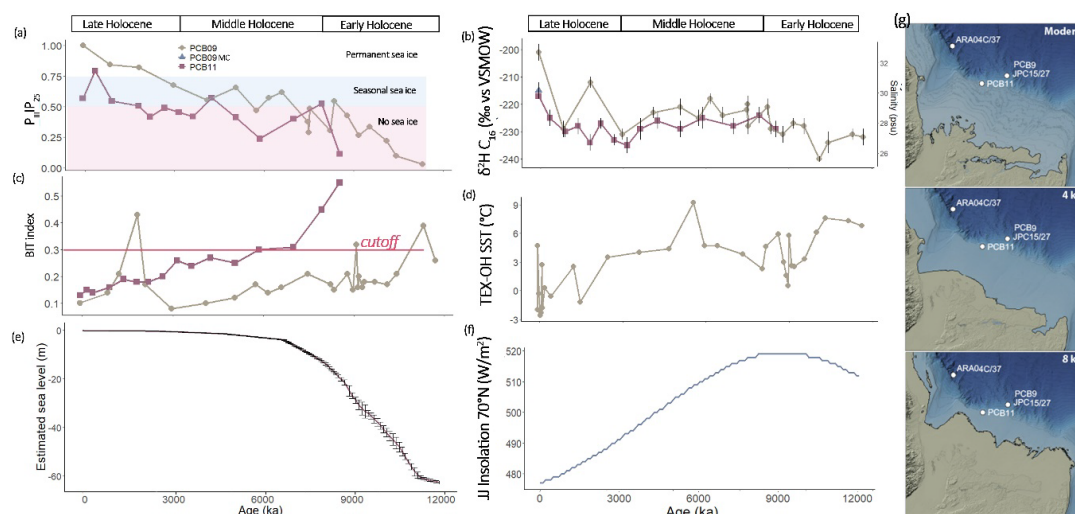
Surface sediments $\delta^2\text{H } C_{16:0}$ values from the Beaufort Sea (Fig. S3) range from -275 to -200‰, comparable with the values obtained by the preliminary study of (Sachs et al., 2018). $\delta^2\text{H } C_{16:0}$ values of all sediments correlate with summer salinity ($r^2 = 0.63$, $p < 0.001$) and the calibration equation is the same as the one obtained by (Sachs et al., 2018). This is to the contrary to what (Allan et al., 2023; J. Wu et al., 2025) observed in a set of surface sediments in Baffin Bay and a downcore record of the Beaufort Sea, where no relationship with salinity is observed. This contrast for the surface sediments could come from the different environment as Baffin Bay is a much more enclosed basin compared to the Beaufort Sea, or that $\delta^2\text{H } C_{16:0}$ values encompassed a too small range of salinity (31 – 33 psu).

Sea surface salinity inferred from $\delta^2\text{H } C_{16:0}$ values at PCB09 increased from $27 \text{ psu} \pm 7$ during the Early Holocene to $30 \pm 7 \text{ psu}$ during the Middle Holocene, and remained stable until 3 ka, increasing to $32 \pm 7 \text{ psu}$ during the Late Holocene (Fig. 4b). Reconstructed salinity at PCB11 was more stable during the Middle Holocene and Late Holocene ($28 \pm 7 \text{ psu}$) until an increase to $30 \pm 7 \text{ psu}$ in the last centuries. (Fig. 4b). This is in agreement with modern observation showing lower salinities at PCB11 than around PCB09 (Fig. S2).



Two different set of SSTs were reconstructed using the OH-GDGT only (RI-OH') or a combination of OH- and isoGDGT (TEX-OH) (Fig. 4d, Fig. S5a,b). SSTs were only reconstructed when BIT index were below 0.3 as both calibration are sensitive to terrestrial input (Varma et al., 2025). TEX-OH reconstructed SSTs in PCB09 varied between $7 \pm 2.6^\circ\text{C}$ in the Early Holocene to $0 \pm 2.6^\circ\text{C}$ between 1-1.5 ka, and reach modern values of $3 \pm 2.6^\circ\text{C}$ toward present (Fig. 4d). RI-OH' reconstructed SSTs in PCB09 give unrealistic values between 7 and 10 ka whereas PCB11 reconstructed SST is stable around 3°C (Fig. S5b). PCB11 TEX-OH reconstructed SSTs are stable during the Early to Middle Holocene ($\sim 5.0 \pm 2.6^\circ\text{C}$). However, reconstruction after 1 ka give large unrealistic variation ($5-15^\circ\text{C}$, Fig. S5a).

The BIT index showed a steady decrease in PCB11 throughout the Holocene and until 5 ka in PCB09 (Fig. 4c). In PCB09, this decrease was interrupted at 1 ka with BIT index values reaching 0.4. This increase was likely due to a relative decrease in crenarchaeol concentration (Fig. S5a) whereas brGDGT concentration did not decrease significantly (Fig. 4i).



313

Figure 4: Reconstructed environmental parameters for PCB9 (red circles) and PCB11 (brown squares) (a) $P_{III}IP_{25}$ (PIP_{25} calculated with HBI III as phytoplankton biomarker), (b) δ^2H of $C_{16:0}$ fatty acid and corresponding reconstructed salinity (Sachs et al., 2018), (c) BIT index (Hopmans et al., 2004), (d) sea surface temperature derived from TEX-OH (Varma et al., 2024), (e), global sea level estimates derived from Lambeck et al., (2014) and (f) June-July (JJ) insolation at 70°N (Laskar et al., 2004). Panel g) Illustrative examples of plaeoshorelines at 8 and 4 ka compared to the modern. These were generated by adjusting the sea-level using the modern bathymetry portrayed in IBCAO V. 5 (Jakobsson et al., 2024). Relative sea-level adjustments were taken from ICE 6G_C (Peltier et al., 2015) for the grid cell encompassing the position of PCB11. The sea-level adjustments for this location were 46 m at 8 ka and 12 m at 4 ka (Figure S7).



323

324 3.6. Micropaleontology

325 Almost all of the planktonic foraminifera (99-100% in abundance relative to other species) observed in PCB09 are *N.*
 326 *pachyderma*, formerly *N. pachyderma sinistra*. This is expected since this species has been found to dominate polar
 327 water masses (e.g. Eynaud 2011; Moller, Schulz, and Kucera 2013). Planktonic foraminifera are mostly absent in
 328 PCB11, consistent with data from plankton tows indicating that planktic foraminifera are rare on the Canadian shelf
 329 where surface waters are influenced by Mackenzie River discharge (Vilks, 1989). In PCB09, the foraminiferal shells
 330 appear white and fragmented in sections with abundant light-colored and sand-sized ice-rafted debris and other detrital
 331 materials (Fig. S6). Foraminifera are more abundant in samples that have relatively more mud aggregates than sand-
 332 sized debris (Fig. 2a,b). There is almost zero accumulation rate (per mm yr⁻¹) of *N. pachyderma* within the shelf slope
 333 from 10 ka.

334 4. Discussion

335 This study aims to reconstruct Holocene paleoenvironmental conditions in the southeastern Beaufort Sea focusing on
 336 spatial variability between the shelf slope (> 500m water depth) and the outer shelf (<100 m water depth). By analyzing
 337 the abundance and ratios of sea ice biomarkers (IP₂₅, HBI II), phytoplankton and heterotrophic archaeal productivity
 338 markers (HBI III, HBI IV, iso- and OH-GDGT), terrestrial inputs (brGDGTs, terrestrial sterols), and reconstructed
 339 environmental indicators (salinity, SST) this study aim to highlight spatial environmental difference between a shallow
 340 (PCB11) and deep (PCB09) site. In the following sections, we interpret biomarker records in a chronological
 341 framework, highlighting the dynamic relationship between freshwater inputs, ocean circulation, and sea ice conditions.

342 4.1. Deglacial to Early Holocene (12 – 8.5 ka)

343 The Deglacial to Early Holocene is only recorded at the shelf slope location. This period is characterized by low
 344 concentrations of sea ice biomarkers resulting in low PIP₂₅ values (Fig. 3a,b, Fig. 4a). The low concentration means
 345 that this area had some sea ice coverage during the Deglacial to Early Holocene, but the presence of HBI III and HBI
 346 IV (Fig. 3e,f) indicate that the region was only under seasonal ice cover until spring allowing late spring/summer
 347 open-water diatom primary production (Belt et al., 2015). Heterotrophic production in the shelf slope region during



348 this period is relatively low (as suggested by the presence of ammonium oxidizer Thaumarchaea-derived isoGDGTs)
349 but increased and peaked at 8.2 ka. During 12 – 8.5 ka, SST are elevated in comparison with the rest of the Holocene
350 (Fig. 4d) which coincided with peak summer insolation (Fig. 4f) (Laskar et al., 2004). The warmer surface waters
351 might have inhibited the development of sea ice over the Beaufort Shelf.

352 During the Deglacial to Early Holocene, large freshwater inputs to the Beaufort Shelf, inferred from the low
353 reconstructed salinity (Fig. 4b) likely originated from the decaying Laurentide Ice Sheet. Such water masses derived
354 from drainage regions that had undergone minimal weathering would have released low amounts of nutrients. The
355 influx of low-salinity freshwater may have intensified salinity-driven stratification on the shelf, reducing the upwelling
356 of nutrient-rich saline Pacific waters to the surface which also limited nutrient availability. This stratification and less
357 nutrient availability likely limited primary productivity and the presence of ammonia-oxidizers on the Beaufort Shelf.
358 It is important to note that sea level on the Beaufort Shelf was >60 m lower in the Early Holocene than what it is today
359 (Fig. 4e,g). Implying that between 10-12 ka, the Beaufort Sea was a shallow estuarine environment (Fig. 4g, Hill et
360 al., 1993).

361 The concentration of brGDGTs and terrestrial sterols in the shelf slope location during the Early Holocene peaked at
362 11.3 and 8.2 ka (Fig. 3i,j), which agrees with an inflow from the LIS and freshly deglaciated surfaces as seen in nearby
363 cores (Klotsko et al., 2019; J. Wu et al., 2020). Additionally, increased freshwater input may have transported more
364 detrital calcium (Ca), as indicated by elevated Ca/Ti ratios (Fig. 2a), which could have enhanced the preservation of
365 foraminifera by buffering the water column and limiting carbonate dissolution, in sediments along the shelf slope.
366 Murton et al. (2010) used optically stimulated luminescence (OSL) dating to identify two major meltwater pulses
367 through the Mackenzie River system between 13 and 11.7 ka and between 11.7 and 9.3 ka. This timing is supported
368 by sedimentary and isotopic records from the Beaufort Sea indicating a major Lake Agassiz flood route through the
369 Mackenzie system (Keigwin et al., 2018; Klotsko et al., 2019). These meltwater events coincide with events (11.3,
370 8.2 ka) in the biomarker records from this study, and one event at 10.1 ± 0.4 ka is recorded in the reconstructed salinity
371 (Fig. 4b), suggesting enhanced freshwater forcing contributed to disrupted ocean circulation and increased sea ice
372 extent. The massive meltwater discharge from the LIS (at least ~ 9000 km³) into its surrounding oceans have been the
373 major cause for eustatic sea level rise from 10 to 6 ka (Moran & Bryson, 1969).



374 **4.2. Middle to Late Holocene (8.5 – 0 ka)**

375 After 8.5 ka, a major cooling in SST was recorded at the slope (6 to 3 °C, Fig. 4d), sea ice biomarkers showed a steady
376 increase in the slope and outer shelf areas (Fig. 3c,d). These trends were reflected in the PIP₂₅ values (Fig. 4a), where
377 both locations started experiencing increasing sea ice cover after 8.5 ka with stable sea ice-edge or polynya conditions
378 present at the shelf slope by 7 – 6 ka (Fig. 4a). On the outer shelf, as shown in PCB11, sea ice biomarker concentration
379 increased along with open water diatom biomarkers. As PCB11 was very close to land before 6 ka (Fig. 4g), it is likely
380 that the sea ice biomarkers originated from landfast ice diatoms. Between 4 -6 ka, PCB11 was likely in a “flaw-lead”
381 position between landfast ice and sea ice, as recorded nowadays 80 km from shore (Fig. S1) (Carmack et al., 2004).
382 PIP₂₅ (Fig. 4a) in PCB11 is lower than in PCB09, indicating that stable sea ice conditions on the outer shelf were only
383 reached after 4 ka, 2 ky later than on the slope. This delay is likely due to the position of PCB11, close to the coast
384 and in the flaw-lead zone. In summary, during 8-3 ka, PCB11 was in a flaw-lead position or under landfast ice,
385 enabling enhanced productivity despite increasing sea ice cover at the shelf slope.

386 In the Late Holocene, i.e. 3 ka to present, sea ice cover became permanent over the shelf slope as indicated by higher
387 PIP₂₅ values (>0.8), increased reconstructed salinity (Fig. 4a,b), as well as a decreased amount of open water diatom
388 (Fig. 3e,f). A sharp decrease in PIP₂₅ at 1.5 ka, in parallel of a steep decrease in open-water diatom biomarkers indicate
389 a permanent sea ice cover at the shelf slope. This permanent sea ice cover occurred during a sharp decline in SST to
390 0 °C (Fig. 4d). Heterotrophic (ammonia oxidizer) production was inhibited, likely due to strong stratification of the
391 water column or the presence of an ammonium-depleted water mass. This indicated a migration of the sea ice edge
392 shoreward and a change in oceanic conditions between 1.5-0.4 ka. This period coincides with the Little Ice Age (Mann
393 et al., 2009), when the region experienced a prolonged cold interval and the nutrient-rich Pacific water inflow was
394 reduced (Falardeau et al., 2022). The permanent sea-ice cover was also likely restricting shelf-break upwelling of
395 nutrient-rich deeper water (Schulze & Pickart, 2012), reducing primary productivity. At the outer shelf, seasonal sea
396 ice conditions continued to expand and became fully established after 2 ka.



410 The nearby cores JPC15 (Keigwin et al., 2018), ARAC20 (J. Wu et al., 2020) (Fig. 1) recorded similar environmental
411 changes (sea ice cover, freshwater input) as in PCB09 but different from those recorded in the shallow PCB11 site,
412 highlighting the differences between shelf break and outer shelf and the spatial variation of the polynya position. Aside
413 from the close by cores (Keigwin et al., 2018; Klotsko et al., 2019; J. Wu et al., 2020), other Arctic records in the
414 Canadian Archipelago (Vare et al., 2009), East Siberian (Dong et al., 2022), Kara (Hörner et al., 2018) , Chukchi
415 (Stein et al., 2017), Laptev (Fahl & Stein, 2012; Hörner et al., 2016), and Lincoln (Detlef et al., 2023) Seas and along
416 the Lomonosov Ridge (Stein & Fahl, 2012), report minimum sea-ice cover during the Early Holocene (centred around
417 10 ka) (Fig. 5). Norther Greenland(Detlef et al., 2023) and the Laptev Sea (Fahl & Stein, 2012; Hörner et al., 2016)
418 are the first regions to record permanent sea-ice cover after the Early Holocene minimum, around 9 ka. The Beaufort
419 Sea (this study, J. Wu et al., 2020) showed permanent sea-ice cover on the shelf break after 3 ka. Seasonal sea-ice
420 cover in the shallower region of the Laptev and Beaufort Seas (PS51-159 and PCB11) was recorded after 5 and 3 ka,
421 respectively. The Chukchi Sea (ARA2B) had seasonal sea-ice throughout after 8 ka, with an increase after 4.5 ka
422 (Stein et al., 2017). The variations in sea ice cover and primary production in the Chukchi Sea were attributed to
423 differences in solar insolation and variability in Pacific water inflow, which brought increased heat flux and episodic
424 declines in sea ice cover. In the Canadian Archipelago, a record that did not include the Early Holocene (Belt et al.,
425 2010; Vare et al., 2009) reported an increased sea ice cover from 7 to 3 ka. Along the Lomonosov Ridge, Stein & Fahl
426 (2012) described extended sea ice cover after 9 ka. Detlef et al. (2023) reconstructed sea ice conditions from a sediment
427 core covering the last 11 ka, showing that while the Lincoln Sea currently experiences perennial sea ice cover, it
428 underwent a shift to seasonal sea ice during the Early Holocene (around 10 ka) due to significantly warmer conditions.
429 This period of reduced sea ice cover is associated with increased marine productivity and meltwater input indicated
430 by biomarker and sedimentary features.

431 In contrast, studies using dinocyst assemblages from around the Arctic Ocean (see the review of de Vernal et al., 2013)
432 report constant sea ice cover for the Early to Middle Holocene with a clear decrease around 6 ka, followed by a return
433 to pre-6 ka conditions until an increase toward modern times. This could be due to a warm-bias in the dinocyst estimate
434 or a non-representative training set (de Vernal et al., 2013).

435 Together, many of the biomarker studies provide a consistent narrative of (spring) sea ice development during the
436 Holocene across the Arctic Ocean. The transition from largely open-water and freshwater-influenced conditions



437 during the Deglacial to Early Holocene to increasing sea ice cover from the Middle Holocene onward is a shared
438 feature across the Arctic shelf seas, although spatial and local variations in ice dynamics and productivity are observed
439 due to local freshwater input and warm current inflow.

440 **5. Conclusion**

441 Analysis of two sediment cores from the outer Beaufort Shelf and shelf slope help elucidate the region's
442 paleoenvironmental variability throughout the Holocene. The shelf slope had ice-free conditions and minimal sea ice
443 extent during the Deglacial to Early Holocene. During the Early Holocene, the Beaufort Shelf was ~60 m shallower
444 than today, and experienced large freshwater influxes due to the decaying LIS. The following sea level rise brought
445 the core sites further away from the river mouth and eroding permafrost coasts, lowering the input of terrestrial organic
446 matter. The insolation-based cooling recorded during the beginning of the Middle Holocene drove the increase in sea
447 ice cover for the Beaufort Shelf and other Arctic marginal seas. Sea-ice cover and its impact on local upwelling and
448 regional Pacific inflow impacted local primary production, concentrating the phytoplankton production in open-water
449 flaw-lead or polynya conditions. Open water conditions substantially decreased during the Late Holocene as extended
450 sea ice cover developed during the Little Ice Age at the shelf slope, which caused primary productivity to further
451 decline. This study highlights the similarities in sea ice variability across Arctic marginal seas, implying alike factors
452 driving sea ice variability and the impending loss of perennial sea ice condition as our modern climate approaches
453 thermal conditions similar or above the Early Holocene.

454 **Data availability**

455 The research data are submitted and under review on the Bolin Center database.

456 **Author contribution** MS - Data Curation, Formal analysis, Investigation, Writing – original draft preparation, LBr
457 Conceptualization, Supervision, Funding acquisition, Writing – review & editing, MO Resource, Funding acquisition,
458 Investigation, Writing – review & editing IH Conceptualization, Supervision, Writing – review & editing, TT
459 Resource, Writing – review & editing LBi Investigation, NH Resource, Writing – review & editing, DN Resource,
460 Writing – review & editing, MF Funding acquisition, Writing – review & editing, JL Conceptualization, Funding
461 acquisition, Investigation, Project administration, Supervision, Writing – review & editing



462 **Competing interest** The authors declare that they have no conflict of interest.

463 **Acknowledgments**

464 We thank Amundsen Science and ArcticNet for their support in preparing the cruise and the crew of the CCGS
465 Amundsen and the PeCaBeau team for their help during sampling. We thank the Alfred Wegener Institute for
466 providing the multicorer and part of the logistical support. Carina Johansson is thanked for her help with XRF analysis,
467 and Axel Birkholz and Thomas Kuhn for the bulk elemental and isotopic analysis. MS was funded through a SNSF-
468 Ambizione (PZ00P2-209012) to JL. The ship-time leading to sample acquisition for this study was funded by the
469 European Union H2020 as part of the EU Project ARICE (grant agreement n° 730965) with additional support from
470 the Swiss Polar Institute (Project number PAF-2020-004).

471



472 **References**

- 473 Belt, Simon T., Guillaume Massé, Steven J. Rowland, Michel Poulin, Christine Michel, and Bernard LeBlanc. 2007.
474 “A Novel Chemical Fossil of Palaeo Sea Ice: IP₂₅.” *Organic Geochemistry* 38 (January): 16–27.
475 <https://doi.org/10.1016/j.orggeochem.2006.09.013>.
- 476 Belt, Simon T., and Juliane Müller. 2013. “The Arctic Sea Ice Biomarker IP₂₅: A Review of Current Understanding,
477 Recommendations for Future Research and Applications in Palaeo Sea Ice Reconstructions.” *Quaternary Science*
478 *Reviews* 79 (November): 9–25. <https://doi.org/10.1016/j.quascirev.2012.12.001>.
- 479 Broecker, Wallace S., James P. Kennett, Benjamin P. Flower, James T. Teller, Sue Trumbore, Georges Bonani, and
480 Willy Wolfli. 1989. “Routing of Meltwater from the Laurentide Ice Sheet During the Younger Dryas Cold Episode.”
481 *Nature* 341 (September): 318–21. <https://doi.org/10.1038/341318a0>.
- 482 Brown, T. A., S. T. Belt, A. Tatarek, and C. J. Mundy. 2014. “Source Identification of the Arctic Sea Ice Proxy IP₂₅.”
483 *Nature Communications* 5 (June): 4197. <https://doi.org/10.1038/ncomms5197>.
- 484 Buizert, Christo, Vasileios Gkinis, Jeffrey P. Severinghaus, Feng He, Benoit S. Lecavalier, Philippe Kindler, Markus
485 Leuenberger, et al. 2014. “Greenland Temperature Response to Climate Forcing During the Last Deglaciation.”
486 *Science* 345 (September): 1177–80. <https://doi.org/10.1126/science.1254961>.
- 487 Carlson, Anders E., Allegra N. LeGrande, Delia W. Oppo, Rosemarie E. Came, Gavin A. Schmidt, Faron S. Anslow,
488 Joseph M. Licciardi, and Elizabeth A. Obbink. 2008. “Rapid Early Holocene Deglaciation of the Laurentide Ice
489 Sheet.” *Nature Geoscience* 1 (9): 620–24. <https://doi.org/10.1038/ngeo285>.
- 490 Carmack, EC, RW Macdonald, and S Jasper. 2004. “Phytoplankton Productivity on the Canadian Shelf of the Beaufort
491 Sea.” *Marine Ecology Progress Series* 277: 37–50. <https://doi.org/10.3354/meps277037>.
- 492 Dai, Aiguo, Dehai Luo, Mirong Song, and Jiping Liu. 2019. “Arctic Amplification Is Caused by Sea-Ice Loss Under
493 Increasing CO₂.” *Nature Communications* 10 (January): 121. <https://doi.org/10.1038/s41467-018-07954-9>.
- 494 Data, I. E. 2021) National Snow and Ice Data Center. <https://nsidc.org/>



- 495 Detlef, Henrieka, Matt O'Regan, Christian Stranne, Mads Mørk Jensen, Marianne Glasius, Thomas M. Cronin, Martin
496 Jakobsson, and Christof Pearce. 2023. "Seasonal Sea-Ice in the Arctic's Last Ice Area During the Early Holocene."
497 *Communications Earth & Environment* 4 (1). <https://doi.org/10.1038/s43247-023-00720-w>.
- 498 Eicher, O.; Baumgartner, M.; Schilt, A.; Schmitt, J.; Schwander, J.; Stocker, T.F.; Fischer, H. (2016-10-06):
499 NOAA/WDS Paleoclimatology - NGRIP Ice Core 120,000 Year Total Air Content Data. [indicate subset used].
500 NOAA National Centers for Environmental Information. <https://doi.org/10.25921/n0d0-ng26>. Accessed [July 2023].
- 501 Eynaud, Frédérique. 2011. "Planktonic Foraminifera in the Arctic: Potentials and Issues Regarding Modern and
502 Quaternary Populations." *IOP Conference Series: Earth and Environmental Science* 14 (May): 012005.
503 <https://doi.org/10.1088/1755-1315/14/1/012005>.
- 504 Fietz, Susanne, Sze Ling Ho, and Carme Huguet. 2020. "Archaeal Membrane Lipid-Based Paleothermometry for
505 Applications in Polar Oceans." *Oceanography* 33 (June). <https://doi.org/10.5670/oceanog.2020.207>.
- 506 Frey, K. E., J. C. Comiso, L. W. Cooper, J. M. Grebmeier, and L. V. Stock. 2020. "Arctic Ocean Primary Productivity:
507 The Response of Marine Algae to Climate Warming and Sea Ice Decline - NOAA Arctic — arctic.noaa.gov."
508 [https://arctic.noaa.gov/Report-Card/Report-Card-2020/ArtMID/7975/ArticleID/900/Arctic-Ocean-Primary-](https://arctic.noaa.gov/Report-Card/Report-Card-2020/ArtMID/7975/ArticleID/900/Arctic-Ocean-Primary-Productivity-The-Response-of-Marine-Algae-to-Climate-Warming-and-Sea-Ice-Decline)
509 [Productivity-The-Response-of-Marine-Algae-to-Climate-Warming-and-Sea-Ice-Decline](https://arctic.noaa.gov/Report-Card/Report-Card-2020/ArtMID/7975/ArticleID/900/Arctic-Ocean-Primary-Productivity-The-Response-of-Marine-Algae-to-Climate-Warming-and-Sea-Ice-Decline).
- 510 Häkkinen, Sirpa. 1987. "Upwelling at the Ice Edge: A Mechanism for Deep Water Formation?" *Journal of*
511 *Geophysical Research* 92 (C5): 5031. <https://doi.org/10.1029/jc092ic05p05031>.
- 512 Hartman, Julian D., F. Sangiorgi, M. A. Barcena, F. Tateo, F. Giglio, S. Albertazzi, F. Trincardi, P. K. Bijl, L. Langone,
513 and A. Asioli. 2021. "Sea-Ice, Primary Productivity and Ocean Temperatures at the Antarctic Marginal Zone During
514 Late Pleistocene." *Quaternary Science Reviews* 266 (August): 107069.
515 <https://doi.org/10.1016/j.quascirev.2021.107069>.
- 516 Herfort, Lydie, Stefan Schouten, Ben Abbas, Marcel J. W. Veldhuis, Marco J. L. Coolen, Cornelia Wuchter, Jan P.
517 Boon, Gerhard J. Herndl, and Jaap S. Sinninghe Damste. 2007. "Variations in Spatial and Temporal Distribution of
518 Archaea in the North Sea in Relation to Environmental Variables." *FEMS Microbiology Ecology* 62 (3): 242–57.
519 <https://doi.org/10.1111/j.1574-6941.2007.00397.x>.



- 520 Hill, Philip R., Arnaud Héquette, and Marie-Hélène Ruz. 1993. “Holocene Sea-Level History of the Canadian Beaufort
521 Shelf.” *Canadian Journal of Earth Sciences* 30 (1): 103–8. <https://doi.org/10.1139/e93-009>.
- 522 Huguet, C., Kim, J., Sinninghe Damsté, J. S., and Schouten, S. 2006: Reconstruction of sea surface temperature
523 variations in the Arabian Sea over the last 23 kyr using organic proxies (TEX86 and U37K’), *Paleoceanography*, 21,
524 <https://doi.org/10.1029/2005pa001215>.
- 525 Hopmans, Ellen C, Johan W. H Weijers, Enno Schefuß, Lydie Herfort, Jaap S Sinninghe Damsté, and Stefan Schouten.
526 2004. “A Novel Proxy for Terrestrial Organic Matter in Sediments Based on Branched and Isoprenoid Tetraether
527 Lipids.” *Earth and Planetary Science Letters* 224 (July): 107–16. <https://doi.org/10.1016/j.epsl.2004.05.012>.
- 528 Kashiwase, Haruhiko, Kay I. Ohshima, Sohey Nihashi, and Hajo Eicken. 2017. “Evidence for Ice-Ocean Albedo
529 Feedback in the Arctic Ocean Shifting to a Seasonal Ice Zone.” *Scientific Reports* 7 (August): 8170.
530 <https://doi.org/10.1038/s41598-017-08467-z>.
- 531 Keigwin, L. D., S. Klotsko, N. Zhao, B. Reilly, L. Giosan, and N. W. Driscoll. 2018. “Deglacial Floods in the Beaufort
532 Sea Preceded Younger Dryas Cooling.” *Nature Geoscience* 11 (8): 599–604. [https://doi.org/10.1038/s41561-018-](https://doi.org/10.1038/s41561-018-0169-6)
533 0169-6.
- 534 Lake, Robert Alan. 1967. “Heat Exchange Between Water and Ice in the Arctic Ocean.” *Archiv Für Meteorologie,*
535 *Geophysik Und Bioklimatologie Serie A* 16 (October): 242–59. <https://doi.org/10.1007/BF02246401>.
- 536 Laskar, J., P. Robutel, F. Joutel, M. Gastineau, A. C. M. Correia, and B. Levrard. 2004. “A Long-Term Numerical
537 Solution for the Insolation Quantities of the Earth.” *Astronomy & Astrophysics* 428 (December): 261–85.
538 <https://doi.org/10.1051/0004-6361:20041335>.
- 539 Lattaud, J., Bröder, L., Haghipour, N., Rickli, J., Giosan, L., and Eglinton, T. I. 2021. Influence of Hydraulic
540 Connectivity on Carbon Burial Efficiency in Mackenzie Delta Lake Sediments, *Journal of Geophysical Research:*
541 *Biogeosciences*, 126. <https://doi.org/10.1029/2020jg006054>.
- 542 Leri, A. C., Mayer, L. M., Thornton, K. R., and Ravel, B. 2014. Bromination of marine particulate organic matter
543 through oxidative mechanisms, *Geochimica et Cosmochimica Acta*, 142, 53–63,
544 <https://doi.org/10.1016/j.gca.2014.08.012>.



- 545 Liu, Xiao-Lei, Julius S. Lipp, Jeffrey H. Simpson, Yu-Shih Lin, Roger E. Summons, and Kai-Uwe Hinrichs. 2012.
546 “Mono- and Dihydroxyl Glycerol Dibiphytanyl Glycerol Tetraethers in Marine Sediments: Identification of Both Core
547 and Intact Polar Lipid Forms.” *Geochimica Et Cosmochimica Acta* 89 (July): 102–15.
548 <https://doi.org/10.1016/j.gca.2012.04.053>.
- 549 Lü, Jun-Mei, Seong-Joong Kim, Ayako Abe-Ouchi, Yongqiang Yu, and Rumi Ohgaito. 2010. “Arctic Oscillation
550 During the Mid-Holocene and Last Glacial Maximum from PMIP2 Coupled Model Simulations.” *Journal of Climate*
551 23 (14): 3792–3813. <https://doi.org/10.1175/2010jcli3331.1>.
- 552 Lü, Xiaoxia, Xiao-Lei Liu, Felix J. Elling, Huan Yang, Shucheng Xie, Jinming Song, Xuegang Li, Huamao Yuan,
553 Ning Li, and Kai-Uwe Hinrichs. 2015. “Hydroxylated Isoprenoid GDGTs in Chinese Coastal Seas and Their Potential
554 as a Paleotemperature Proxy for Mid-to-Low Latitude Marginal Seas.” *Organic Geochemistry* 89-90 (December): 31–
555 43. <https://doi.org/10.1016/j.orggeochem.2015.10.004>.
- 556 Marcott, Shaun A., Jeremy D. Shakun, Peter U. Clark, and Alan C. Mix. 2013. “A Reconstruction of Regional and
557 Global Temperature for the Past 11,300 Years.” *Science* 339 (March): 1198–1201.
558 <https://doi.org/10.1126/science.1228026>.
- 559 Matero, I. S. O., L. J. Gregoire, R. F. Ivanovic, J. C. Tindall, and A. M. Haywood. 2017. “The 8.2 Ka Cooling Event
560 Caused by Laurentide Ice Saddle Collapse.” *Earth and Planetary Science Letters* 473 (September): 205–14.
561 <https://doi.org/10.1016/j.epsl.2017.06.011>.
- 562 McNichol, A. P., E. A. Osborne, A. R. Gagnon, B. Fry, and G. A. Jones. 1994. “TIC, TOC, DIC, DOC, PIC, POC —
563 Unique Aspects in the Preparation of Oceanographic Samples for 14C-AMS.” *Nuclear Instruments and Methods in*
564 *Physics Research Section B: Beam Interactions with Materials and Atoms* 92 (1–4): 162–65.
565 [https://doi.org/10.1016/0168-583x\(94\)95998-6](https://doi.org/10.1016/0168-583x(94)95998-6).
- 566 Moller, Tobias, Hartmut Schulz, and Michal Kucera. 2013. “The Effect of Sea Surface Properties on Shell Morphology
567 and Size of the Planktonic Foraminifer *Neoglobobulimina* *Pachyderma* in the North Atlantic.” *Palaeogeography,*
568 *Palaeoclimatology, Palaeoecology* 391 (December): 34–48. <https://doi.org/10.1016/j.palaeo.2011.08.014>.



- 569 Moran, Joseph M., and Reid A. Bryson. 1969. "The Contribution of Laurentide Ice Wastage to the Eustatic Rise of
570 Sea Level: 10, 000 to 6, 000 BP." *Arctic and Alpine Research* 1 (2): 97. <https://doi.org/10.2307/1550016>.
- 571 Müller, Juliane, Kirstin Werner, Ruediger Stein, Kirsten Fahl, Matthias Moros, and Eystein Jansen. 2012. "Holocene
572 Cooling Culminates in Sea Ice Oscillations in Fram Strait." *Quaternary Science Reviews* 47 (July): 1–14.
573 <https://doi.org/10.1016/j.quascirev.2012.04.024>.
- 574 Murton, Julian B., Mark D. Bateman, Scott R. Dallimore, James T. Teller, and Zhirong Yang. 2010. "Identification
575 of Younger Dryas Outburst Flood Path from Lake Agassiz to the Arctic Ocean." *Nature* 464 (7289): 740–43.
576 <https://doi.org/10.1038/nature08954>.
- 577 NGRIP-Members. 2004. "High-Resolution Record of Northern Hemisphere Climate Extending into the Last
578 Interglacial Period." *Nature* 431 (7005): 147–51. <https://doi.org/10.1038/nature02805>.
- 579 Not, Christelle, and Claude Hillaire-Marcel. 2012. "Enhanced Sea-Ice Export from the Arctic During the Younger
580 Dryas." *Nature Communications* 3 (January): 647. <https://doi.org/10.1038/ncomms1658>.
- 581 Omstedt, Anders, Eddy C. Carmack, and Robie W. Macdonald. 1994. "Modeling the Seasonal Cycle of Salinity in
582 the Mackenzie Shelf/Estuary." *Journal of Geophysical Research* 99: 10011. <https://doi.org/10.1029/94JC00201>.
- 583 Park, Hyo-Seok, Seong-Joong Kim, Andrew L. Stewart, Seok-Woo Son, and Kyong-Hwan Seo. 2019. "Mid-Holocene
584 Northern Hemisphere Warming Driven by Arctic Amplification." *Science Advances* 5 (12).
585 <https://doi.org/10.1126/sciadv.aax8203>.
- 586 Pfalz, Gregor, Bernhard Diekmann, Johann-Christoph Freytag, Liudmila Syrykh, Dmitry A. Subetto, and Boris K.
587 Biskaborn. 2022. "Improving Age–Depth Relationships by Using the LANDO ('Linked Age and Depth Modeling')
588 Model Ensemble." *Geochronology* 4 (1): 269–95. <https://doi.org/10.5194/gechron-4-269-2022>.
- 589 Pickart, Robert S. 2004. "Shelfbreak Circulation in the Alaskan Beaufort Sea: Mean Structure and Variability."
590 *Journal of Geophysical Research* 109: C04024. <https://doi.org/10.1029/2003JC001912>.



- 591 Rantanen, Mika, Alexey Yu. Karpechko, Antti Lipponen, Kalle Nordling, Otto Hyvärinen, Kimmo Ruosteenoja, Timo
592 Vihma, and Ari Laaksonen. 2022. “The Arctic Has Warmed Nearly Four Times Faster Than the Globe Since.”
593 *Communications Earth & Environment* 3 (August): 168. <https://doi.org/10.1038/s43247-022-00498-3>.
- 594 Richter, T. O., Gaast, S. van der, Koster, B., Vaars, A., Gieles, R., Stigter, H. C. de, Haas, H. De and Weering, T. C.E.
595 van. 2005. The Avaatech XRF Core Scanner: technical description and applications to NE Atlantic sediments, Geol
596 Soc. London, Spec. Publ., 267(1), 39–50, doi:10.1144/GSL.SP.2006.267.01.03.
- 597 Sachs, J. P., Stein, R., Maloney, A. E., Wolhowe, M., Fahl, K., and Nam, S.-i. 2018. An Arctic Ocean paleosalinity
598 proxy from $\delta^2\text{H}$ of palmitic acid provides evidence for deglacial Mackenzie River flood events, Quaternary Science
599 Reviews, 198, 76–90, <https://doi.org/10.1016/j.quascirev.2018.08.025>.
- 600 Schouten, Stefan, Ellen C. Hopmans, and Jaap S. Sinninghe Damsté. 2013. “The Organic Geochemistry of Glycerol
601 Dialkyl Glycerol Tetraether Lipids: A Review.” *Organic Geochemistry* 54 (January): 19–61.
602 <https://doi.org/10.1016/j.orggeochem.2012.09.006>.
- 603 Schouten, Stefan, Ellen C. Hopmans, Enno Schefuß, and Jaap S. Sinninghe Damsté. 2002. “Distributional Variations
604 in Marine Crenarchaeotal Membrane Lipids: A New Tool for Reconstructing Ancient Sea Water Temperatures?”
605 *Earth and Planetary Science Letters* 204 (November): 265–74. [https://doi.org/10.1016/S0012-821X\(02\)00979-2](https://doi.org/10.1016/S0012-821X(02)00979-2).
- 606 Serreze, Mark C., and Jennifer A. Francis. 2006. “The Arctic Amplification Debate.” *Climatic Change* 76 (June):
607 241–64. <https://doi.org/10.1007/s10584-005-9017-y>.
- 608 Sinninghe Damsté, Jaap S., W. Irene C. Rijpstra, Marco J. L. Coolen, Stefan Schouten, and John K. Volkman. 2007.
609 “Rapid Sulfurisation of Highly Branched Isoprenoid (HBI) Alkenes in Sulfidic Holocene Sediments from Ellis Fjord,
610 Antarctica.” *Organic Geochemistry* 38 (1): 128–39. <https://doi.org/10.1016/j.orggeochem.2006.08.003>.
- 611 Smith, Richard W., Thomas S. Bianchi, and Xinxin Li. 2012. “A Re-Evaluation of the Use of Branched GDGTs as
612 Terrestrial Biomarkers: Implications for the BIT Index.” *Geochimica Et Cosmochimica Acta* 80 (March): 14–29.
613 <https://doi.org/10.1016/j.gca.2011.11.025>.
- 614 Steenfelt, A., Thomassen, B., Lind, M. and Kyed, J.: Karrat. 1998. reconnaissance mineral exploration in central West
615 Greenland, Geol. Greenl. Surv. Bull., 180, 73–80.



- 616 Stein, Ruediger, Kirsten Fahl, Paul Gierz, Frank Niessen, and Gerrit Lohmann. 2017. “Arctic Ocean Sea Ice Cover
617 During the Penultimate Glacial and the Last Interglacial.” *Nature Communications* 8 (August): 373.
618 <https://doi.org/10.1038/s41467-017-00552-1>.
- 619 Stein, Ruediger, and Robie W. MacDonald, eds. 2004. *The Organic Carbon Cycle in the Arctic Ocean*. Springer Berlin
620 Heidelberg. <https://doi.org/10.1007/978-3-642-18912-8>.
- 621 Stoll, Heather M., Isabel Cacho, Edward Gasson, Jakub Sliwinski, Oliver Kost, Ana Moreno, Miguel Iglesias, et al.
622 2022. “Rapid Northern Hemisphere Ice Sheet Melting During the Penultimate Deglaciation.” *Nature Communications*
623 13: 3819. <https://doi.org/10.1038/s41467-022-31619-3>.
- 624 Teller, James T. 2013. “Lake Agassiz During the Younger Dryas.” *Quaternary Research* 80: 361–69.
625 <https://doi.org/10.1016/j.yqres.2013.06.011>.
- 626 Ullman, David J., Anders E. Carlson, Steven W. Hostetler, Peter U. Clark, Joshua Cuzzone, Glenn A. Milne, Kelsey
627 Winsor, and Marc Caffee. 2016. “Final Laurentide Ice-Sheet Deglaciation and Holocene Climate-Sea Level Change.”
628 *Quaternary Science Reviews* 152: 49–59. <https://doi.org/10.1016/j.quascirev.2016.09.014>.
- 629 Vernal, Anne de, Claude Hillaire-Marcel, Cynthia Le Duc, Philippe Roberge, Camille Brice, Jens Matthiessen, Robert
630 F. Spielhagen, and Ruediger Stein. 2020. “Natural Variability of the Arctic Ocean Sea Ice During the Present
631 Interglacial.” *Proceedings of the National Academy of Sciences* 117: 26069–75.
632 <https://doi.org/10.1073/pnas.2008996117>.
- 633 Wu, Junjie, Ruediger Stein, Kirsten Fahl, Nicole Syring, Seung-Il Nam, Jens Hefter, Gesine Mollenhauer, and Walter
634 Geibert. 2020. “Deglacial to Holocene Variability in Surface Water Characteristics and Major Floods in the Beaufort
635 Sea.” *Communications Earth & Environment* 1: 27. <https://doi.org/10.1038/s43247-020-00028-z>.